JVI Journals.ASM.org

A Stabilized Headless Measles Virus Attachment Protein Stalk Efficiently Triggers Membrane Fusion

Melinda A. Brindley,[a] Rolf Suter,[a] Isabel Schestak,[a] Gabriella Kiss,[b] Elizabeth R. Wright,[b] Richard K. Plemper[a,b]

Center for Inflammation, Immunity & Infection, Georgia State University, Atlanta, Georgia, USA[a]; Division of Pediatric Infectious Diseases, Department of Pediatrics, Emory University School of Medicine and Children's Healthcare of Atlanta, Atlanta, Georgia, USA[b]

Paramyxovirus attachment and fusion (F) envelope glycoprotein complexes mediate membrane fusion required for viral entry. The measles virus (MeV) attachment (H) protein stalk domain is thought to directly engage F for fusion promotion. However, past attempts to generate truncated, fusion-triggering-competent H-stem constructs remained fruitless. In this study, we addressed the problem by testing the hypothesis that truncated MeV H stalks may require stabilizing oligomerization tags to maintain intracellular transport competence and F-triggering activity. We engineered H-stems of different lengths with added 4-helix bundle tetramerization domains and demonstrate restored cell surface expression, efficient interaction with F, and fusion promotion activity of these constructs. The stability of the 4-helix bundle tags and the relative orientations of the helical wheels of H-stems and oligomerization tags govern the kinetics of fusion promotion, revealing a balance between H stalk conformational stability and F-triggering activity. Recombinant MeV particles expressing a bioactive H-stem construct in the place of full-length H are viable, albeit severely growth impaired. Overall, we demonstrate that the MeV H stalk represents the effector domain for MeV F triggering. Fusion promotion appears linked to the conformational flexibility of the stalk, which must be tightly regulated in viral particles to ensure efficient virus entry. While the pathways toward assembly of functional fusion complexes may differ among diverse members of the paramyxovirus family, central elements of the triggering machinery emerge as highly conserved.

The paramyxovirus family comprises major human pathogens such as the parainfluenzaviruses (PIVs), mumps virus, measles virus (MeV), and respiratory syncytial virus (RSV). Of these, members of the *Paramyxovirinae* subfamily infect cells through a concerted action of two envelope glycoprotein complexes, the F protein and the attachment protein. H-type proteins are exclusively found in the morbillivirus genus, which includes MeV, while other *Paramyxovirinae* genera feature hemagglutinin (HA)-neuraminidase (HN) or glycoprotein (G)-type attachment proteins (1). Irrespective of actual enzymatic activity, all *Paramyxovirinae* attachment proteins contain β-barrel head domain structures characteristic of sialidases (1, 2). The binding sites for the viral receptors reside in these head structures (3–9), which are connected to the transmembrane domains through helical stalks (1, 10).

Structural and biochemical studies have demonstrated that the tetramer represents the physiological oligomer of the MeV attachment protein (4, 11). Furthermore, crystal structures of the Newcastle disease virus (NDV) and PIV5 HN stalk domains revealed a 4-helix bundle organization (12, 13). This stalk configuration is likely conserved among *Paramyxovirinae* family members, since engineered disulfide bonds in the MeV H stalk can result in the formation of covalently linked tetramers (14, 15) and some H variants with substantial stalk extension through insertion of helix repeat elements remained bioactive (16).

For viral entry, the attachment protein specifically activates the homotypic F protein upon receptor binding (17–19). Assuming an initial metastable prefusion conformation, irreversible refolding of triggered F trimers into a stable postfusion form then mediates merger of the viral envelope with cellular membranes, resulting in fusion pore formation (20, 21). Specificity for homotypic F proteins resides in the attachment protein stalk domain (10, 22–25), and a defined candidate F contact zone was identified in the MeV H stalk (16, 26). In addition, a truncated PIV5 HN protein stem lacking the head domains was recently shown to maintain F-triggering activity, suggesting a modular organization of the protein into a regulatory, receptor binding head region and the F-contacting stalk effector domain (27). Remarkably, however, a panel of previously generated headless MeV H-stem constructs was, unlike the analogous PIV5 HN stem, intracellularly retained and F activation defective (28), raising the issue of whether fundamental differences between individual *Paramyxovirinae* genera exist in the fusion-triggering mechanism.

Despite a high degree of conservation of central structural features and biochemical properties of diverse *Paramyxovirinae* envelope glycoproteins (reviewed in references 1, 10, and 29), recent studies revealed additional differences in the formation of fusion complexes between members of the morbillivirus genus and paramyxoviruses with HN-type attachment proteins. Morbillivirus H tetramers interact tightly with the homotypic F trimers in the secretory system and the plasma membrane of the host cell (30–32). Fusion complex formation is independent of receptor binding (14), suggesting that the proposed F interaction sites in the H stalk are permanently accessible for docking. In contrast, backfolding of the head domains onto the equivalent sites in the HN stalks was proposed to prevent interaction with F prior to receptor binding (27). Rather, interaction with the receptor is thought to induce a rearrangement of the HN head domains that opens up the contact zone for transient binding of prefusion F.

Received 15 July 2013 **Accepted** 17 August 2013

Published ahead of print 21 August 2013

Address correspondence to Richard K. Plemper, rplemper@gsu.edu.

M.A.B. and R.S. contributed equally to this article.

doi:10.1128/JVI.01945-13

This model is supported by crystal structures of HN ectodomains suggesting distinct head-to-stalk arrangements (8, 12, 13) and efficient fusion activation by the headless PIV5 HN stalk construct (27).

To explore whether the mechanism of morbillivirus H-mediated F-triggering is fundamentally distinct from HN-type fusion activation, we have in this study tested the hypothesis that MeV H stalks, in contrast to HN stalk proteins, assemble into loosely arranged helical bundles that require the presence of the head domains for structural stabilization. To evaluate the role of regulated F activation in the context of virus infection, we examined the ability of appropriately stabilized MeV H-stems to sustain productive viral entry through random F triggering.

MATERIALS AND METHODS

Cell culture, transfection, and virus stocks. Baby hamster kidney cells (C-13; ATCC) stably expressing T7 polymerase (BSR-T7/5; 33), African green monkey kidney epithelial cells (CCL-81; ATCC) stably expressing human signaling lymphocytic activation molecule (Vero/hSLAM; 34), canine signaling lymphocytic activation molecule (Vero/cSLAM; 35), or canine distemper virus (CDV) H and cSLAM (Vero-CDV-H/cSLAM; 36), and HEK293T cells (CRL-11268; ATCC) were maintained at 37°C and 5% CO_2 in Dulbecco's modified Eagle's medium supplemented with 7.5% fetal bovine serum. Stably transfected cell lines were incubated in the presence of G-418 (2.5 mg/ml) every fifth passage. In some content-mixing experiments, CO_2-independent medium supplemented with 7.5% fetal bovine serum was employed. Cells were transfected using either Lipofectamine 2000 (Invitrogen) or, for virus recovery transfections, calcium phosphate precipitation (Promega). Standard virus stocks were prepared by infecting Vero/hSLAM cells at a multiplicity of infection (MOI) of 0.001 50% tissue culture infective dose ($TCID_{50}$)/cell, followed by incubation at 37°C. Cell-associated progeny particles were released through freeze/thaw procedures and titers determined by $TCID_{50}$ as described previously (37).

Molecular biology. The basis for all H expression constructs was a previously described pCG-H_{Flag} plasmid encoding an H protein with a triple Flag epitope tag added to the cytosolic H amino terminus (11). GCN4 tandem-stop cassettes were introduced through PCR-based modification using appropriate primers followed by religation of the amplicons. The QuikChange protocol (Stratagene) was employed for all subsequent site-directed mutagenesis steps. The integrity of all constructs was verified through DNA sequencing. To generate recombinant MeV (recMeV) genomes, the H-L intergenic region was added to the H-122stemGCN-Δ15 gene through PCR modification and religation. The resulting H-stem expression cassette was liberated through PacI SpeI restriction digest and used to replace the H-encoding open reading frame in a plasmid containing a cDNA copy of the MeV-Edmonston (Edm) genome (38). The enhanced green fluorescent protein (eGFP) open reading frame was then inserted through transfer of a NotI-SacII fragment of a genomic plasmid containing the recMeV-GFP sequence (39).

Recombinant MeV. RecMeV-H-122stemGCHN-Δ15 particles were generated using a modified recovery protocol as described previously (16). Emerging infectious particles were transferred onto Vero/hSLAM cells, followed by repeated passaging. For stock production, infectious centers were subsequently transferred to Vero-CDV-H/cSLAM cells and cell-associated particles harvested when extensive cell-to-cell fusion was detected. Prior to all experiments, virus grown on Vero-CDV-H/cSLAM cells was passaged through Vero/cSLAM cells to generate progeny particles lacking CDV H protein. To confirm the integrity of the recombinant viruses, RNA was extracted from virus stock using an RNeasy minikit (Qiagen) and cDNAs created using random hexamer primers and Superscript II reverse transcriptase (RT; Invitrogen). Modified genome regions were amplified using appropriate primers. The generation and recovery of H stalk extended recMeV-H-(118▽41x) were previously described (16). For affinity grids, modified recMeVs harboring triple Flag or triple Flag/His tandem epitope tags affixed to the carboxy terminus of the H protein were generated.

Purification of MeV particles for cryo-electron microscopy (cryo-EM). For virus production, 10 15-cm-diameter dishes of Vero/hSLAM cells were infected with the recMeV variant at an MOI of 0.005 $TCID_{50}$/cell. Viral particles were collected when the cells showed more than 90% syncytia, approximately 4 days postinfection. Supernatants were clarified of cellular debris through a 0.45-μM-pore-size filter and polyethylene glycol (PEG) precipitated by adding 10% PEG 8000 and 2% NaCl to the final volume of the virus-containing solution. Viral particles were pelleted by centrifugation at 8,000 × *g* for 1.5 h at 4°C, and the virus/PEG pellet was resuspended in TNE buffer (10 mM Tris, pH 7.5; 100 mM NaCl; 1 mM EDTA). The material was layered on a 20% to 60% sucrose cushion in TNE buffer and centrifuged at 100,000 × *g* for 1.5 h, and viral particles were collected from the interface of the 20% to 60% sucrose layers. To reduce the quantity of sucrose in the sample, the recovered virus-containing fraction was diluted in TNE buffer and centrifuged at 100,000 × *g* for 20 min. The pellets were resuspended in TNE buffer and repelleted as described above. The resulting final pellets (approximate yields, 10^7 $TCID_{50}$/ml) were resuspended in 200 μl TNE buffer.

Cryo-EM affinity grids, microscopy, and image processing. Quantifoil R1.2/1.3 carbon-copper grids were treated with ethyl acetate to remove plastic film residues. A 20% nickel-nitrilotriacetic acid (Ni-NTA)-containing lipid monolayer was attached to the copper back side of the grid for greater stability. Aliquots (4 μl) of His-tagged protein A (Abcam) were applied to the monolayer and incubated for 1 min. The excess solution was pipetted away. Immediately, 4 μl of specific antibodies directed against the Flag (M2; Sigma) epitope tag was applied to the grids for 1 min. The excess solution was pipetted away. The virus sample (4 μl) was added to the grid and allowed to attach for 1 min. A second aliquot of the virus specimen was mixed in a 1:1 ratio with the bovine serum albumin (BSA)-treated 10-nm-diameter gold particles in a total volume of 2.5 μl and applied to the grid. After blotting, grids were plunge-frozen using a Mark III Vitrobot (FEI).

Vitrified specimens were imaged on a Jeol JEM-2200FS, 200-kV field emission gun-transmission EM (FEG-TEM) with an in-column Omega energy filter operated at a slit width of 20 eV. Images on the JEOL JEM-2200FS TEM were collected with a Gatan US4000 charge-coupled-device (CCD) camera (4k by 4k). Images were automatically binned by two and acquired with a pixel size equal to or less than 7.6 Å. For the tilt series acquisition, a cumulative electron dose of ~120 $e^-/Å^2$ was distributed over a tilt series ranging from −62° to +62°. Images were acquired at −4.0-μm defocus (first contrast transfer function [CTF] zero, 0.31 nm^{-1}). Tilt series images were automatically collected with 2° of angular increments using the predictive SerialEM package (40).

Three-dimensional reconstructions (tomograms) were generated from the aligned image stacks using IMOD Version 4.3.1 (41). Tomograms were noise reduced by nonlinear anisotropic diffusion as implemented in Bsoft (42) and virions segmented using the Amira 5.4.1 software package segmentation tool (Visualization Sciences Group).

Cell-to-cell fusion microphotographs. Fluorescence microscopy was performed with a Zeiss Axio Observer D.1 inverted microscope. For phase-contrast images, a Nikon Diaphot 200 inverted microscope was employed. In both cases, a 10× objective was used.

Surface biotinylation, SDS-PAGE, and antibodies. Protein surface expression was determined as described before (43) with the following modifications. 293T cells (6×10^5 per well in a 6-well plate format) were transfected with 3 μg of plasmid DNA encoding the specified MeV H construct. Washed cells were biotinylated with 0.5 mg/ml sulfosuccinimidyl-2-(biotinamido)ethyl-1,3-dithiopropionate (Pierce), quenched, and subjected to precipitation using immobilized streptavidin (GE Healthcare) after lysis in radioimmunoprecipitation assay (RIPA) buffer (1% sodium deoxycholate, 1% NP-40, 150 mM NaCl, 50 mM Tris-Cl [pH 7.2],

10 mM EDTA, 50 mM sodiumfluoride, protease inhibitors [Roche], 1 mM phenylmethylsulfonyl fluoride). Washed precipitates were fractioned through gel electrophoresis on 4% to 20% TGX gels (Bio-Rad) and transferred to polyvinylidene difluoride (PVDF) membranes (GE Healthcare), and H protein material was detected through decoration with specific antibodies directed against the Flag epitope tags (M2; Sigma). Immunoblots were developed using a ChemiDoc digital imaging system (Bio-Rad). The Image Lab package (Bio-Rad) was used for densitometry. In all quantitations and immunoblots shown, standard H was fractionated on the same gel.

Dual split-protein cell content-mixing assay. 293T effector cells were transfected with plasmids encoding the Dsp_{1-7} dual split-protein component (44), H-stem, and MeV F. 293T target cells received plasmid DNA encoding the Dsp_{8-11} subunit. Premature effector cell fusion was suppressed through addition of 25 μM fusion inhibitory peptide (FIP) (Bachem). Cells were washed 16 to 24 h posttransfection, both populations combined at equal ratios, and mixed cells transferred to solid-wall 96-well plates. Reconstitution of renilla luciferase as a marker for cell content mixing was assessed continuously at 37°C, using the EnduRen (Promega) life cell substrate and a Synergy H1 (BioTek) multifunction microplate reader. In the experiments that included standard H, results of individual experiments were normalized for the peak value of the H data set, followed by averaging of the normalized values. The averages of relative H max values do not reach 100% at any time, since peak values of standard H controls are not reached at exactly identical time points in individual experiments.

Regression modeling. Normalized and averaged cell content-mixing assay data were analyzed using a logistic model. An initial offset of 0.5 h was added *in silico* (two data points) to generate defined starting points for modeling based on the value of the first measured data point. The decay phase was determined for each construct individually based on the decline of consecutive data points and was excluded from regression modeling. Curve fitting was based on the following modified logistic equation: relative luciferase units (RLU) = $A/\{1 + \exp[4 \times \mu_m/A \times (\lambda - t) + 2]\}$ (45). Curve fitting was carried out in the Prism 5 software package (GraphPad), and the maximal increase in RLU values (maximal rate [μ_m]) and highest absolute RLU values (peak A) were extracted (λ, lag time).

Statistical analysis. To assess the statistical significance of differences between sample means, unpaired two-tailed *t* tests were applied using the Prism 5 (GraphPad) or Excel (Microsoft) software package. For statistical analysis of coimmunoprecipitation, surface expression, and F-triggering data sets, the Pearson product-moment correlation coefficient (46, 47) was calculated to test a linear correlation between the data sets. Influential outliers (i.e., data points that, when excluded, substantially increased the r^2 value of the regression analysis) were removed from the regression line calculations. In the surface versus coimmunoprecipitation data set, only the H-(F111A)-122stemGCN-Δ15 control was identified as an influential outlier, whereas, in the F-triggering versus coimmunoprecipitation data set, the H-(I98A)-122stemGCN-Δ15 control and H-$122stem^{-1}$GCN-Δ15 qualified as influential outliers. One standard deviation above and below the regression line was considered within a confidence interval for the assay.

Envelope glycoprotein cross-linking and immunoprecipitation. MeV glycoprotein coimmunoprecipitation was performed as described previously (16) with the following modifications. 293T cells (6×10^5 per well in a 6-well plate format) were transfected with 1.5 μg each of plasmid DNAs encoding carboxy-terminally HA epitope-tagged MeV F and the specified H construct. After incubation in the presence of 100 μM FIP for 30 h, washed cells were treated with 3,3′-dithiobis[sulfosuccinimidylpropionate] (DTSSP; Pierce) cross-linker at a 1 mM final concentration, followed by quenching and lysis in RIPA buffer. Cleared lysates were subjected to immunoprecipitation using anti-Flag antibodies and matrix-immobilized protein G and washed precipitates subjected to SDS-PAGE and immunoblotting. Coprecipitated F protein material was visualized through decoration of immunoblots with specific antibodies directed against the HA epitope tag (16B12; Abcam) and chemiluminescence-based densitometric quantification.

Virus neutralization assays. Recombinant MeV-GFP or recMeV-H-122stem stocks were incubated with the MeV neutralizing antibody (E81) (48), isotype control (M2), or FIP for 15 min at room temperature. The mixture was spinoculated (1,500 rpm for 45 min at 4°C) onto 293T cells, and plates were incubated at 37°C. At 6 h postinfection, FIP was added to prevent the formation of excessive syncytia. The number of green cells was enumerated and compared to mock-treated control numbers after 48 h of incubation.

RESULTS

Efficient fusion activation by the previously described, stalk-extended MeV H variants (16) suggested that F triggering does not require direct contacts between the H and F head domains in addition to the H stalk-to-F interaction when the elongated stalk sections protrude perpendicularly from the membrane. To test this experimentally, we collected tilt series of cryopreserved standard and recombinant MeV particles that harbor the stalk-extended H protein in place of normal H (16). The three-dimensional reconstructions (tomograms) revealed a dense glycoprotein arrangement on the MeV surface (Fig. 1A), in good agreement with recently reported reconstructions of standard MeV particles (49). In the modified recMeV-H-(118▽41x), glycoprotein electron density extended from the viral envelope by approximately an additional 6 nm (Fig. 1B), which closely matches the hypothetical pitch of the 41-residue helical element inserted into the H stalk (16) (Fig. 1C). These findings indicate that efficient MeV F triggering may indeed be achieved in the absence of direct contacts between the glycoprotein head domains, prompting us to evaluate the molecular basis for the lack of bioactivity of the previously generated MeV H-stems (28).

GCN4 zipper domain-stabilized H-stems are F triggering competent. Assuming a helical coiled-coil organization of the MeV H stalk, intracellular retention of these H-stems may reflect an inherently weaker helix bundle arrangement of morbillivirus H than PIV5 HN stalks. To test this prediction, we generated a terminal tetramerization module (GCN) based on a derivative of the leucine-zipper domain of the yeast GCN4 transcriptional activator, which spontaneously assembles into a parallel 4-helix bundle (50), followed by tandem-stop codons. This cassette was inserted into the H stalk downstream of residue 122, 133, or 158 (Fig. 1C). The first insertion site was chosen based on its position downstream of the proposed H-F interaction domain (16), and the other two flank naturally occurring cysteine residues at H stalk positions 139 and 154, which both engage in intermolecular disulfide bonds for covalent H dimerization (28).

When we coexpressed the resulting H-stems with MeV F, both H-122stemGCN and H-133stemGCN were, in contrast to H-158stemGCN, capable of productive F triggering, as indicated by the formation of multinucleated giant cells or syncytia (Fig. 1D). However, the onset and growth of these syncytia lagged behind those observed in control cells expressing standard H and F. We have previously reported that non-GCN4 zipper-stabilized MeV H-stems ending in the immediate vicinity of H-133 or downstream of the H disulfide bonds between residues 139 and 154 are intracellularly retained (28). Consistent with these findings, a newly generated non-GCN4 zipper-stabilized H-122stem was also not F triggering competent (Fig. 1D).

The molecular design of the GCN4 zipper clamp governs F triggering. Quantitation of relative plasma membrane steady-state levels of the three H-stem constructs revealed efficient sur-

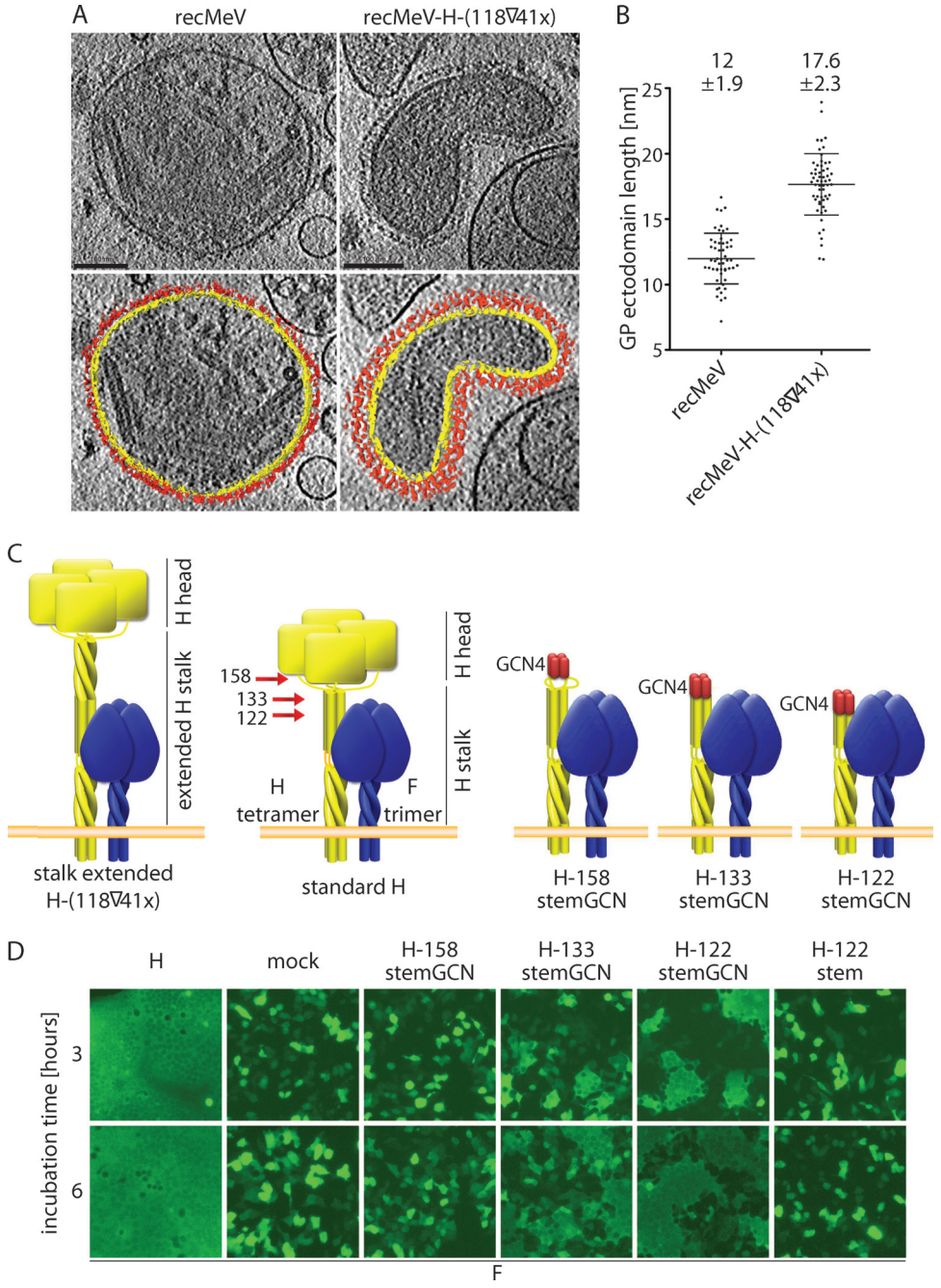

FIG 1 Direct contact of MeV H head domains with F is not required for fusion triggering. (A) Three-dimensional tomographic reconstructions and segmentations of measles virions. (Upper panels) Tomographic sections (~18 nm thick) through the centers of standard and H stalk-extended MeV particles. (Lower panels) In segmentations, the viral membrane is represented in yellow and the envelope glycoproteins are represented in red. Scale bars, 100 nm. (B) Measurements of the height of the surface glycoprotein (GP) ectodomains from the top of the viral membrane. Numbers indicate average heights of 55 (recMeV) or 58 [H-(118∇41x] measurements ± standard deviations (SD). (C) Schematic of H stalk extended (16) (left), standard H stalk (center), and the three truncated H-stems (right). F trimers are shown for comparison, and numbers mark the stalk lengths of the alternative H-stems explored. (D) Syncytium formation in cell populations cotransfected with MeV F, an H variant as indicated, and eGFP. Fluorescent microphotographs were taken at the specified time points after washing out of FIP.

face expression of the H-122stemGCN construct, whereas H-133stemGCN was partially and H-158stemGCN predominantly retained (Fig. 2A, left panel). Surface levels of a nonstabilized H-122stem variant were likewise greatly reduced, underscoring that proper MeV H-stem folding into a transport-competent conformation requires GCN4 zipper domain-induced tetramerization (Fig. 2A, right panel).

Based on this initial characterization, we focused in subsequent experiments on H-stems 122 and 133 and employed a kinetic cell-to-cell fusion assay to monitor productive F triggering, resulting

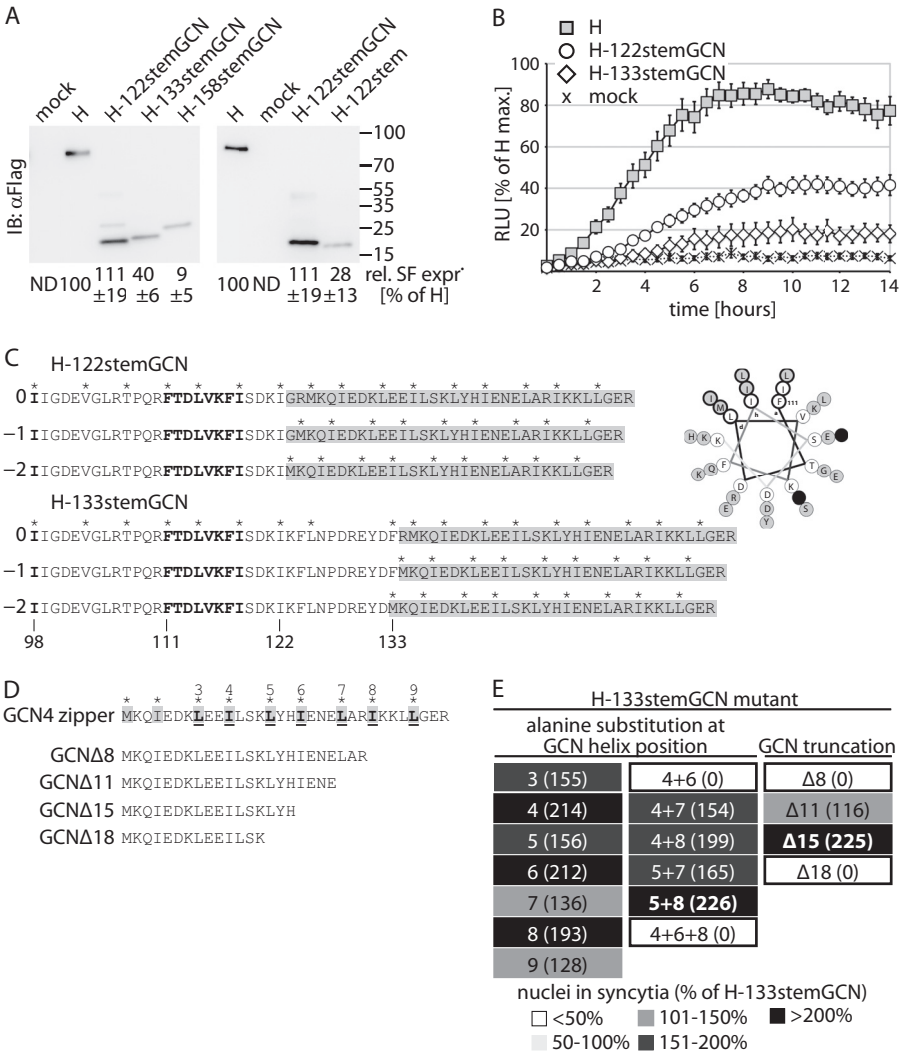

FIG 2 GCN4 zipper domain-stabilized H-stems are intracellular transport and F triggering competent. (A) Surface expression (SF expr.) analysis of the H-stem constructs. Immunoblots (IB) after surface biotinylation were decorated with specific antibodies directed against a Flag epitope tag added to the cytosolic tail of all H constructs. Control cells were transfected with vector DNA only (mock). Numbers represent densitometric quantification relative (Rel.) to standard MeV H. Averages of the results of three independent experiments ± standard errors of the means (SEM) are shown. ND, not determined. (B) Real-time content mixing assay to quantify the kinetic of productive F triggering. Effector cells coexpressing an H variant, F, and one DSP subunit were mixed with target cells expressing the complementary DSP component, and relative luciferase units (RLU) were measured continuously over a 24-h period. Results were normalized for peak values observed with standard H and represent averages of the results of three independent experiments ± SEM. (C) (Left panel) Schematic of the relative helical wheel variations introduced between the H-stem and GCN4 zipper domain. Asterisks above the sequences denote hydrophobic positions in the helix repeat pattern. The numbers "0," "−1," and "−2" refer to the three relative helix positions at the junction. Residues in bold highlight the previously identified F-triggering and F interaction positions. Gray shading marks the GCN4-derived tetramerization tags. (Right panel) Helical wheel projection illustrating the pattern variation at the H-stem/GCN zipper intersection by the example of H-122stemGCN. The projection commences at H residue 111. Hydrophobic helix positions (a, d, h) are highlighted. The transition from the predicted 11-mer repeat of the H stalk to the 7-mer repeat of the GCN zipper disrupts the helical pattern (black filled circles). H-stem residues are shown in open circles and GCN residues in gray-shaded circles. (D) Mutagenesis and truncation of the GCN4 zipper domain. Numbered residues (bold, underlined) were mutagenized. Truncations are calculated from the carboxy terminus. (E) GCN-5A8A double mutants and GCN-Δ15 truncations showed the highest F-triggering activities. Values in parentheses represent the extent of fusion relative to that observed for the starting H-133stemGCN construct. Selected modifications with the highest activities are shown in bold.

in content mixing in almost real time. We have established this dual-split protein (DSP) assay for the MeV glycoprotein system (14), which follows the reconstitution of individually expressed chimeric eGFP-Luciferase protein halves upon membrane fusion (44). Both H-stems were F triggering competent in this assay, but maximal fusion rates and relative peak values reached in the assay were substantially reduced compared to those seen with F triggering by standard H (Fig. 2B).

These findings demonstrate that the MeV H-stalk region acts as a necessary and sufficient effector domain for F triggering. The rescue of bioactivity of the H-stems through added tetramerization domains is consistent with a tetrameric organization of the H stalk and reveals, in contrast to the PIV5 HN protein (27), a low intrinsic stability of the MeV H 4-helix bundle.

Based on our recent observation that structural flexibility in the central section of the MeV H stalk is required for F triggering

by full-length H (14, 15), we hypothesized that partially relaxing the clamping effect of the GCN4 zipper domain on the H stalk may maximize the rate of spontaneous F triggering, provided intracellular transport competence is preserved. We pursued two strategies simultaneously to test this notion experimentally: (i) altering the orientations of the predicted helical wheels of H-stems and GCN4 zipper domains relative to each other through deletion of one or two residues at the H stalk-GCN junction (Fig. 2C) and (ii) adjusting the strength of GCN domain oligomerization through shortening of the GCN zipper or directed mutagenesis of residues located at the hydrophobic face of the helices (Fig. 2D).

Prior to fusion kinetics profiling, GCN domain mutants in the H-133stemGCN background were prescreened microscopically after cotransfection with MeV F (Fig. 2E). The GCN domain modifications of each series associated with the visually highest extent of cell-to-cell fusion were then rebuilt in the H-122stem context, each in all three helical wheel junction variations, and subjected to in-depth characterization.

Optimizing the rate of spontaneous F triggering. Of the three helical wheel variants of the H-122stem, those with predicted uninterrupted (original H-122stemGCN) or minimally disturbed (H-122stem^{-2}GCN) helical wheel transitions showed essentially identical F-triggering kinetics, while the H-122stem^{-1}GCN, featuring a stutter in the helical wheel, completely lacked bioactivity (Fig. 3A, left panel). Although the helix pattern leading up to the transition from stalk to GCN appeared less rigid in the H-133stemGCN construct, productive F triggering by both H-133stem^{-1}GCN and H-133stem^{-2}GCN was improved approximately 2-fold compared to that of the original H-133stemGCN construct (Fig. 3A, right panel).

Truncating the carboxy-terminal 15 residues of the GCN zipper domain resulted in a nearly 4-fold increase in F triggering by H-122stemGCN-Δ15 compared to H-122stemGCN, while both H-122stem^{-1}GCN-Δ15 and H-122stem^{-2}GCN-Δ15 completely lost bioactivity (Fig. 3B, left panel). In the H-133stem background, GCN truncations caused a major reduction in F-triggering activity in all three helical wheel variations (Fig. 3B, right panel). GCN mutagenesis boosted bioactivity of the H-122stem series in all helical wheel combinations, but the overall improvement of fusion kinetics remained below that observed with H-122stemGCN-Δ15 (Fig. 3C, left panel). In contrast, the H-133stem^{-1}GCN-5A8A of the equivalent H-133stem series showed an additional (approximately 2-fold) improvement in F triggering compared to the H-133stem^{-1}GCN construct (Fig. 3C, right panel).

Correlation between H-stem intracellular transport competence and triggering activity. For each H-stem truncation set, we selected two complete GCN modification series that contained the constructs with the highest bioactivities for biochemical characterization (Fig. 4A). With the exception of H-122stem^{-2}GCN-Δ15, H-133stemGCN, and 133stemGCN-5A8A, all of the 12 constructs analyzed showed plasma membrane steady-state levels that were at least 70% of that observed for standard H, confirming efficient intracellular transport. When they were subjected to coimmunoprecipitation experiments, we noted efficient physical association of all bioactive H-stems constructs with F (Fig. 4B). Independently of F-triggering activity, all H-stem variants followed a largely linear correlation of relative surface levels and coimmunoprecipitation efficiency (Fig. 4C), indicating that none of the surface-expressed H-stems spontaneously assumed an F binding-incompetent conformation. We have previously reported such a

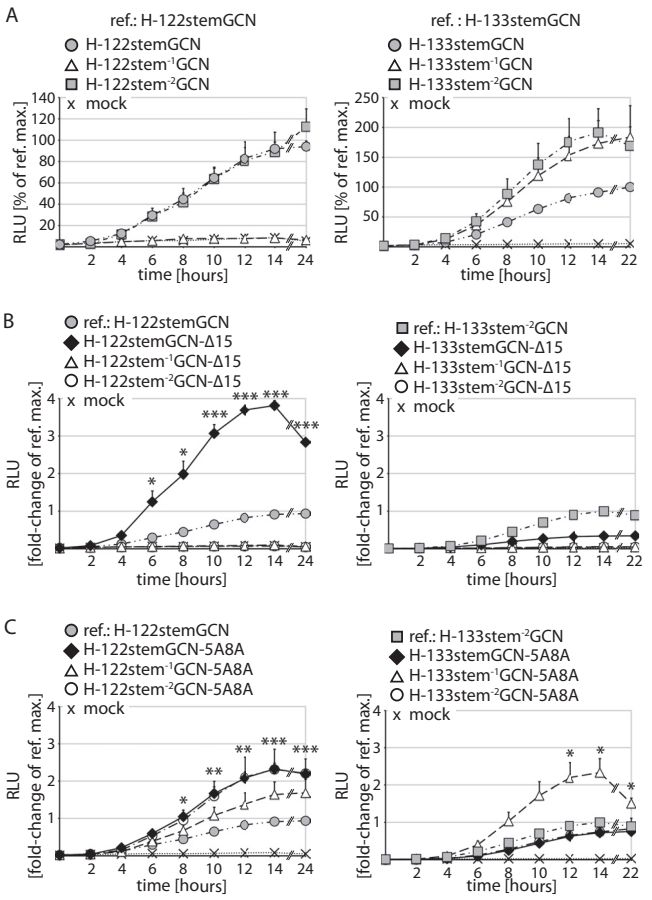

FIG 3 Enhanced F-triggering kinetic through GCN4 zipper domain optimization. (A) Real-time content mixing assays to determine the effect of helical wheel modifications between stems and the tetramerization tag. The original H-stem constructs served as reference (ref.) for data normalization. (B) Assessment of GCN4 zipper domain truncations. (C) GCN4 zipper domain modification through alanine mutagenesis at helix repeat positions 5 and 8 as described for Fig. 2D. For panels B and C, stem constructs with the highest bioactivities identified as described for panel A served as the reference. For panels A to C, values represent averages ± SEM of the results of three independent experiments. Statistical analyses compared optimized and reference (ref.) constructs (*, $P < 0.05$; **, $P < 0.01$; ***, $P < 0.001$). max., maximum.

phenotype for a full-length H carrying an F111A point mutation (14). Plotting F-triggering activity relative to coprecipitation activity, however, illuminated three constructs, H-122stem^{-1}GCN-5A8A, H-122stem^{-1}GCN-Δ15, and H-133stem^{-2}GCN-5A8A, that efficiently (>50% of the level observed for standard H) interacted with F but were overproportionally triggering impaired or defective (Fig. 4D). This profile is reminiscent of the effect of an I98A mutation in full-length H, which tightly interacts with F but does not induce efficient cell-to-cell fusion (51). Introducing the I98A and F111A mutations into the H-122stemGCN-Δ15 background reproduced the previously observed phenotypes (Fig. 4C to E). None of the H-stem constructs showed an overproportional increase in triggering activity relative to interaction with F and surface levels.

The coprecipitation results demonstrate that MeV fusion complexes reside preassembled in the host cell plasma membrane. H and F protein interaction is independent of the presence or absence of the H head domains. Overproportional reduction of trig-

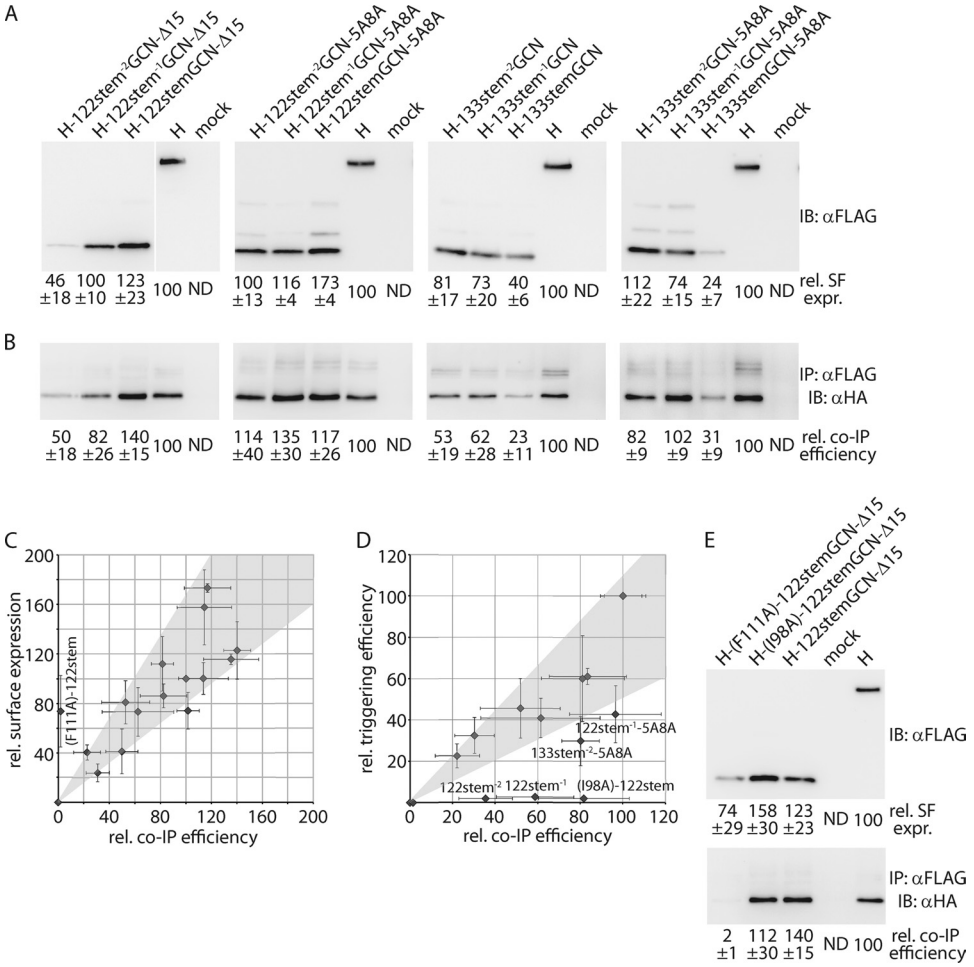

FIG 4 Stabilized H-stem variants are surface expressed and F interaction competent. (A) Surface expression of two complete series of each stem variant, associated with the highest triggering activities. (B) Coimmunoprecipitation (IP) of cross-linked, cell surface-exposed H-F complexes. Immunoblots (IB) were developed with specific antibodies directed against the HA epitope tag, affixed to the cytosolic tail of the F protein. For panels A and B, numbers show densitometry averages ± SEM relative to standard H of the results of three independent experiments. (C) Surface levels of individual H-stems tested as described for panel A directly correlate with co-IP efficiency. Average values obtained as described for panels A and B are plotted. The H-(F122A)-122stemGCN-Δ15 mutant included for control is F binding defective. (D) Several H-stem constructs (specified) are overproportionally F triggering defective. Average kinetic fusion data of the 14-h time points (Fig. 3A to C) are plotted as a function of relative co-IP efficiencies. H-stem122 and H-stem133 series co-IP values were normalized separately for H-122stemGCN-Δ15 and H-133stemGCN-5A8A, respectively. The H-(I98A)-122stemGCN-Δ15 mutant included for control is F triggering defective. Gray areas in panels C and D represent the linear regression line of the data sets ± 1 standard deviation. (E) Surface biotinylation and H-F coprecipitation of the H-122stemGCN-Δ15 (I98A) and (F111A) mutants used as described for panels C and D for control. Numbers represent densitometry averages of the results of three independent experiments ± SEM.

gering activity of several H-stem variants relative to F binding suggests a tight balance between H stalk conformational stability and F activation. These stem constructs may be permanently locked into a transport- and F-docking-competent pretriggering conformation of the MeV H stalk (14).

Mechanistic characterization of an activity-optimized MeV H-stem. To quantify the overall gain in bioactivity through altered design of the tetramerization tags, we tested the most bioactive constructs of each H-stem set, H-122stemGCN-Δ15 and H-133stem^{-1}GCN-5A8A, in kinetic fusion assays (Fig. 5A and B). For each candidate, regression modeling revealed that both the maximal rate and final extent of fusion were significantly increased relative to those of the H-122stemGCN or H-133stemGCN starting constructs (Fig. 5C), but values remained below those observed for standard H.

Concentrating on the more bioactive and shorter H-122stemGCN-Δ15, we assessed the F specificity of the construct through coexpression with MeV F or PIV5 F in BHK cells. Syncytia were readily detectable when PIV5 F and HN were coexpressed or when the H-122stemGCN-Δ15 was combined with MeV F (Fig. 5D). In contrast, coexpression of PIV5 F and the H-122stemGCN-Δ15 did not result in cell-to-cell fusion, indicating specific MeV F triggering by the H-stems. Since BHK cells are MeV receptor negative, expression of standard, full-length MeV H and F likewise did not induce syncytium formation (Fig. 5D). This experiment therefore also confirmed that H-stem-mediated F activation is independent of the presence of standard MeV receptors. However, MeV F and H-122stemGCN-Δ15-mediated syncytium formation remained sensitive to known inhibitors of MeV entry, FIP and the small-molecule F blocker AS-48 (37), demonstrating bona

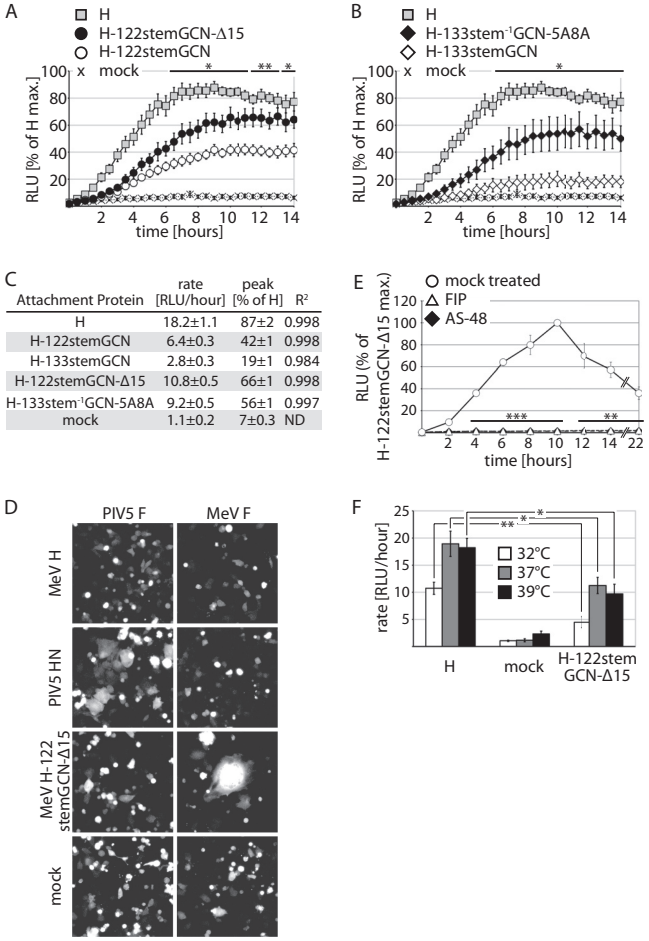

FIG 5 Efficient H-stem-mediated F triggering is receptor independent and MeV F specific. (A and B) Real-time content mixing assay to determine F-triggering kinetics by the optimized H-122stemGCN-Δ15 (A) and H-133stem^{-1}GCN-5A8A (B) stem variants. Values represent averages of the results of three independent experiments ± SEM. Statistical analyses compared the original H-stem construct (Fig. 2A) and optimized H-stem construct (*, $P < 0.05$; **, $P < 0.01$). (C) A logistic regression model was fitted to the fusion kinetic curves shown in panels A and B and Fig. 1D. Maximal triggering rates (rate) and the highest overall activities (peak) ± 95% confidence intervals are shown. R^2, goodness of fit. (D) Cell-to-cell fusion of MeV receptor-deficient BHK cells expressing eGFP and coexpressing MeV H variants or PIV5 HN with either MeV F or PIV5 F. Fluorescence microphotographs are shown. (E) Real-time content-mixing assay of cells coexpressing H-122stemGCN-Δ15 and MeV F in the presence of 100 μM FIP, a 50 μM concentration of the small-molecule MeV entry inhibitor AS-48 (37), or vehicle only (mock treated). Values represent averages of the results of three independent experiments ± SEM. Statistical analyses compared vehicle-treated samples to values obtained after treatment with AS-48 and FIP, respectively (**, $P < 0.01$; ***, $P < 0.001$). (F) Real-time content mixing assay to assess temperature effects on H-122stemGCN-Δ15-mediated F triggering. Three independent experiments were each performed at 32°C, 37°C, and 39°C as indicated, and logistic regression models were fitted to the individual triggering curves. Data represent the mean values of the maximal triggering rates ± SEM (*, $P < 0.05$; **, $P < 0.01$).

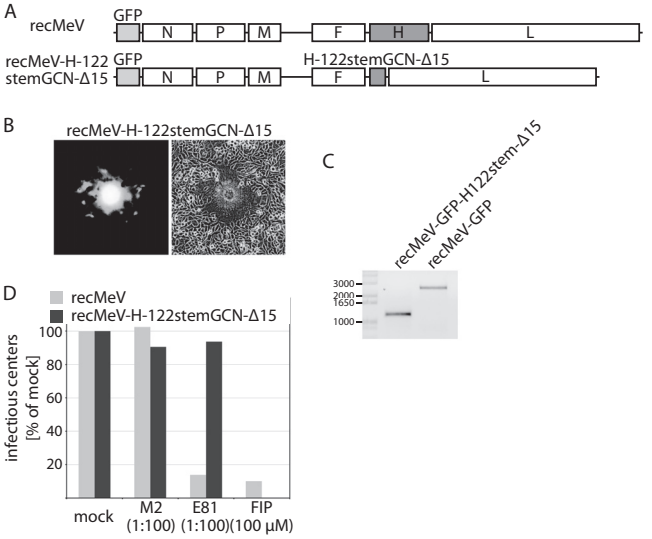

FIG 6 Recombinant MeV expressing the truncated H-122stemGCN-Δ15 attachment protein. (A) Schematic of the standard recMeV and recMeV-H-122stemGCN-Δ15 genomes. Both cDNA constructs harbor an additional eGFP open reading frame in the primary position (light gray). (B) Assessment of cytopathicity induced by recovered recMeV-H-122stemGCN-Δ15 particles 24-h postinfection, using fluorescence and standard microscopy. (C) RT-PCR analysis of the attachment protein-encoding open reading frames after infection of cells with recMeV or recMeV-H-122stemGCN-Δ15. Numbers specify molecular weight of a DNA standard (in bases). (D) recMeV-H-122stemGCN-Δ15 particles are resistant to neutralizing antibodies directed against the H head domain. Virus neutralization assays were conducted using specific monoclonal antibodies (E81 [48]), isotype control antibodies (M2), or FIP. Values represent the amount of infectious fluorescent centers relative to those in cells infected with viruses treated with vehicle (mock) only. Numbers in parentheses specify antibody dilution or FIP concentration.

fide refolding once F was triggered by the H-122stemGCN-Δ15 (Fig. 5E).

To determine whether spontaneous triggering is more closely linked to random molecular motion than to receptor-induced F activation, we assessed the effect of altered incubation temperatures on the kinetics of H-122stemGCN-Δ15-mediated triggering. As expected, the triggering rate was reduced considerably when the temperature was lowered to 32°C (Fig. 5F). However, this was the case for both standard H and H-122stemGCN-Δ15. The differences between the two constructs remained statistically significant, underscoring that no clear distinction in the sensitivities of the two H constructs to altered temperature conditions was detectable. Increasing the incubation temperature to 39°C did not substantially improve the F-triggering rate by either H construct compared to the values obtained at 37°C.

These results confirm a significant increase in F-triggering efficiency through partial truncation or modification of the GCN zipper domain. Fusion activation by H-122stemGCN-Δ15 is receptor independent, but hetero-oligomerization for the formation of functional fusion complexes remains F specific.

Recombinant MeV expressing an H-stem attachment protein. To explore whether spontaneous triggering of cell-to-cell fusion is sufficient to sustain viral entry, we exchanged the H-encoding open reading frame with that of H-122stemGCN-Δ15 in a cDNA copy of the MeV Edmonston strain genome. An additional eGFP open reading frame was inserted at the primary position (Fig. 6A). After rescue transfection for recovery of recMeV-H-122stemGCN-Δ15 particles, infectious centers were detected microscopically based on cytopathicity and eGFP fluorescence (Fig. 6B). These centers were transferrable for successful reinfection of fresh target cells. However, recMeV-H-122stemGCN-Δ15 replication did not result in the extensive cell-to-cell fusion that is characteristic of MeV infections in tissue culture. Titers of infec-

tious particles also remained below 100 $TCID_{50}$ units/ml (compared to the 10^6 to 10^7 $TCID_{50}$ units/ml typically seen with standard recMeV), preventing the generation of virus growth curves.

To verify the molecular nature of the amplified recMeV-H-122stemGCN-Δ15 particles, we analyzed RNA preparations of infected cells by RT-PCR of the H-encoding open reading frame (Fig. 6C) and subjected the virus to neutralization assays. When cells were infected in the presence of neutralizing monoclonal antibodies (E81) that recognize an epitope in the MeV H head domain and efficiently prevent receptor binding of full-length H (48), standard recMeV-GFP was efficiently and specifically neutralized, while entry of recMeV-H-122stemGCN-Δ15 proceeded uninhibited (Fig. 6D). Taken together, these findings confirm receptor-independent entry of recMeV-H-122stemGCN-Δ15 particles. Viral growth is severely impaired in the absence of the H head domains, however, demonstrating that membrane fusion through spontaneous F triggering by H-stems is highly inefficient in the context of virus replication.

DISCUSSION

In this study, we examined basic requirements for productive MeV F triggering in the context of transiently expressed envelope glycoproteins and virus infection. While morbilliviruses, henipaviruses (52), and paramyxoviruses harboring HN-type attachment proteins apparently follow distinct pathways toward the first assembly of functional fusion complexes, our results show that subsequent steps of the F-triggering process are remarkably conserved. The membrane-proximal helical stalk domain of the paramyxovirus attachment protein emerges consistently as the necessary and sufficient effector unit for fusion activation. Reconstructions of cryopreserved MeV recombinants, generation of bioactive headless MeV H variants, and the recovery of infectious particles harboring a truncated H variant support the concept that this model, recently proposed for PIV5 HN (27), equally applies to morbillivirus H.

Tomograms of MeV recombinants revealed that partial duplication of the H stalk indeed raises the H head domains substantially above the viral envelope. Since these elongated H constructs remain capable of efficient F triggering (16), we consider it unlikely that the activation of MeV fusion complexes requires direct functional contacts between the F and H head domains.

Indeed, engineered headless MeV H-stem constructs are capable of efficiently inducing MeV F refolding, provided terminal tetramerization tags are added to the stem. Combined with the recent demonstration that the introduction of cysteine residues into the MeV H stalk can induce covalent H tetramerization (14, 15), this finding furthermore confirms that the 4-helix bundle structure represents the conserved physiological configuration of the paramyxovirus attachment protein stalk. However, the inherent stability of the morbillivirus stalk bundle appears substantially lower than that observed for PIV5 HN, since the latter did not require additional oligomerization tags (27). Partial destabilization of the GCN4-derived 4-helix bundle through point mutations in, or shortening of, the zipper domain significantly enhanced the MeV F-triggering kinetics, indicating that conformational flexibility in the vicinity of the central H stalk section is instrumental for fusion activation. This conclusion is corroborated by our observation that the F-triggering block induced by the engineered disulfide bonds is lifted when H stalk flexibility is restored through reduction of the bonds (14). In contrast to predicting the effect of GCN4 zipper shortening, molecular modeling to estimate the outcome of modifying the relative helical wheel organization of stalk and tag remains inconclusive. We note, however, that the H-122stemGCN variants with an only slightly disrupted helical pattern showed the highest bioactivity levels, while the H-122stem^{-1}GCN constructs featuring a more prominent disruption were either F triggering impaired or defective. However, efficient surface expression and interaction with F of these H-122stem^{-1}GCN constructs argue against gross protein misfolding or presentation of the stalk in a forced post-F-triggering configuration. Rather, disruption of the helical pattern may constrain the H stalk in a pretriggering state (11), limiting the likelihood of spontaneous F activation.

Equally efficient coimmunoprecipitations of F with standard H and bioactive H-stem variants confirmed that MeV fusion complexes assemble in a manner independent of receptor binding, likely in all cases in the secretory system of the host cell (31). This may explain the necessity for conformational flexibility of the morbillivirus H stalk, since the rearrangement of stalk residues located at the H and F interface could serve as the distinctive trigger for F refolding in preassembled complexes. In contrast, HN-type attachment proteins reveal the F attachment sites in the HN stalk only after receptor binding, and the subsequent docking event of HN and F itself could constitute the trigger for F activation. However, a very recently identified mutation rendered an NDV HN protein F binding competent but triggering defective (53), resembling in phenotype the MeV H trigger mutation at stalk position 98 (51). This finding suggests that conformational rearrangements within the attachment protein stalk may, in fact, represent the common molecular trigger for F refolding in all cases.

Despite efficient fusion activation by the H-122stemGCN-Δ15, recombinant MeV harboring this construct was, although viable, severely growth impaired. While the growth phenotype precludes the molecular characterization of the recombinant, this may reflect that the H head domains directly contribute to efficient particle formation or proper particle composition. For many paramyxovirus family members, however, the expression of the matrix and/or F protein results in the efficient formation of virus-like particles (54–56), arguing against this notion. Interestingly, a recent reconstruction of related RSV particles suggested correlated refolding of F proteins present in individual particles (57). Should this be generally applicable to other paramyxovirus family members, MeV recombinants lacking the regulatory H head domains may alternatively encounter an unacceptably high propensity for spontaneous, premature triggering of individual F molecules, resulting in the concerted refolding of the majority of F trimers present on a particle and, consequently, loss of infectivity.

In summary, we illuminate in this study strong parallels between the mechanisms of fusion activation by different paramyxovirus family members. The cellular location and timing for the formation of functional fusion complexes are distinct between different *Paramyxovirinae* genera, but all attachment proteins appear to be organized into a regulatory receptor binding head region and the helical stem effector module. The latter is necessary and sufficient for triggering of PIV5 (27) and MeV F and very likely serves an analogous role in other paramyxovirus fusion systems. Receptor binding-induced or, in the case of H-stem constructs, spontaneous rearrangements of the central MeV H stalk bundle section emerge as the molecular trigger for activation of preassembled MeV fusion complexes. While high levels of spontaneous fusion activation can be achieved in

transient systems, efficient viral entry mandates the presence of the regulatory receptor binding domains of the attachment protein.

ACKNOWLEDGMENTS

We thank A. L. Hammond for comments on the manuscript and J. Holl for help with cryo-EM data analysis. We are grateful to R. A. Lamb for providing PIV5 HN and F expression plasmids, P. Plattet for providing Vero-CDV-H/cSLAM cells, A. Sun for providing AS-48, and N. Kondo and Z. Matsuda for providing dual split-luciferase reporter plasmids.

Electron microscopy was performed with equipment housed in the Emory University Robert P. Apkarian Integrated Electron Microscopy Core, supported, in part, by Emory University, Children's Healthcare of Atlanta, the Center for AIDS Research at Emory University (P30 AI050409), the Georgia Research Alliance, and NSF grant 0923395 (to E.R.W.). This study was supported, in part, by Public Health Service grant AI083402 from the NIH/NIAID (to R.K.P.).

REFERENCES

1. **Lamb RA, Parks GD.** 2007. Paramyxoviridae: the viruses and their replication, p 1449–1496. *In* Knipe DM, Howley PM, Griffin DE, Lamb RA, Martin MA, Roizman B, Straus SE (ed), Fields virology, 5th ed, vol 1. Lippincott Williams & Wilkins, Philadelphia, PA.
2. **Taylor G.** 1996. Sialidases: structures, biological significance and therapeutic potential. Curr. Opin. Struct. Biol. **6:**830–837.
3. **Bowden TA, Aricescu AR, Gilbert RJ, Grimes JM, Jones EY, Stuart DI.** 2008. Structural basis of Nipah and Hendra virus attachment to their cell-surface receptor ephrin-B2. Nat. Struct. Mol. Biol. **15:**567–572.
4. **Hashiguchi T, Ose T, Kubota M, Maita N, Kamishikiryo J, Maenaka K, Yanagi Y.** 2011. Structure of the measles virus hemagglutinin bound to its cellular receptor SLAM. Nat. Struct. Mol. Biol. **18:**135–141.
5. **Lawrence MC, Borg NA, Streltsov VA, Pilling PA, Epa VC, Varghese JN, McKimm-Breschkin JL, Colman PM.** 2004. Structure of the haemagglutinin-neuraminidase from human parainfluenza virus type III. J. Mol. Biol. **335:**1343–1357.
6. **Santiago C, Celma ML, Stehle T, Casasnovas JM.** 2010. Structure of the measles virus hemagglutinin bound to the CD46 receptor. Nat. Struct. Mol. Biol. **17:**124–129.
7. **Xu K, Rajashankar KR, Chan YP, Himanen JP, Broder CC, Nikolov DB.** 2008. Host cell recognition by the henipaviruses: crystal structures of the Nipah G attachment glycoprotein and its complex with ephrin-B3. Proc. Natl. Acad. Sci. U. S. A. **105:**9953–9958.
8. **Yuan P, Thompson TB, Wurzburg BA, Paterson RG, Lamb RA, Jardetzky TS.** 2005. Structural studies of the parainfluenza virus 5 hemagglutinin-neuraminidase tetramer in complex with its receptor, sialyllactose. Structure **13:**803–815.
9. **Zhang X, Lu G, Qi J, Li Y, He Y, Xu X, Shi J, Zhang CW, Yan J, Gao GF.** 2013. Structure of measles virus hemagglutinin bound to its epithelial receptor nectin-4. Nat. Struct. Mol. Biol. **20:**67–72.
10. **Plattet P, Plemper RK.** 2013. Envelope protein dynamics in paramyxovirus entry. mBio **4:**e00413–13. doi:10.1128/mBio.00413-13.
11. **Brindley MA, Plemper RK.** 2010. Blue native PAGE and biomolecular complementation reveal a tetrameric or higher-order oligomer organization of the physiological measles virus attachment protein H. J. Virol. **84:**12174–12184.
12. **Yuan P, Swanson KA, Leser GP, Paterson RG, Lamb RA, Jardetzky TS.** 2011. Structure of the Newcastle disease virus hemagglutinin-neuraminidase (HN) ectodomain reveals a four-helix bundle stalk. Proc. Natl. Acad. Sci. U. S. A. **108:**14920–14925.
13. **Bose S, Welch BD, Kors CA, Yuan P, Jardetzky TS, Lamb RA.** 2011. Structure and mutagenesis of the parainfluenza virus 5 hemagglutinin-neuraminidase stalk domain reveals a four-helix bundle and the role of the stalk in fusion promotion. J. Virol. **85:**12855–12866.
14. **Brindley MA, Takeda M, Plattet P, Plemper RK.** 2012. Triggering the measles virus membrane fusion machinery. Proc. Natl. Acad. Sci. U. S. A. **109:**E3018–E3027.
15. **Ader N, Brindley MA, Avila M, Origgi FC, Langedijk JP, Orvell C, Vandevelde M, Zurbriggen A, Plemper RK, Plattet P.** 2012. Structural rearrangements of the central region of the morbillivirus attachment protein stalk domain trigger F protein refolding for membrane fusion. J. Biol. Chem. **287:**16324–16334.
16. **Paal T, Brindley MA, St Clair C, Prussia A, Gaus D, Krumm SA, Snyder JP, Plemper RK.** 2009. Probing the spatial organization of measles virus fusion complexes. J. Virol. **83:**10480–10493.
17. **Deng R, Mirza AM, Mahon PJ, Iorio RM.** 1997. Functional chimeric HN glycoproteins derived from Newcastle disease virus and human parainfluenza virus-3. Arch. Virol. Suppl. **13:**115–130.
18. **Hu XL, Ray R, Compans RW.** 1992. Functional interactions between the fusion protein and hemagglutinin-neuraminidase of human parainfluenza viruses. J. Virol. **66:**1528–1534.
19. **Morrison T, McQuain C, McGinnes L.** 1991. Complementation between avirulent Newcastle disease virus and a fusion protein gene expressed from a retrovirus vector: requirements for membrane fusion. J. Virol. **65:**813–822.
20. **Lamb RA, Paterson RG, Jardetzky TS.** 2006. Paramyxovirus membrane fusion: lessons from the F and HN atomic structures. Virology **344:**30–37.
21. **Plemper RK.** 2011. Cell entry of enveloped viruses. Curr. Opin. Virol. **1:**92–100.
22. **Lee JK, Prussia A, Paal T, White LK, Snyder JP, Plemper RK.** 2008. Functional interaction between paramyxovirus fusion and attachment proteins. J. Biol. Chem. **283:**16561–16572.
23. **Tanabayashi K, Compans RW.** 1996. Functional interaction of paramyxovirus glycoproteins: identification of a domain in Sendai virus HN which promotes cell fusion. J. Virol. **70:**6112–6118.
24. **Tsurudome M, Kawano M, Yuasa T, Tabata N, Nishio M, Komada H, Ito Y.** 1995. Identification of regions on the hemagglutinin-neuraminidase protein of human parainfluenza virus type 2 important for promoting cell fusion. Virology **213:**190–203.
25. **Deng R, Wang Z, Mirza AM, Iorio RM.** 1995. Localization of a domain on the paramyxovirus attachment protein required for the promotion of cellular fusion by its homologous fusion protein spike. Virology **209:**457–469.
26. **Apte-Sengupta S, Negi S, Leonard VH, Oezguen N, Navaratnarajah CK, Braun W, Cattaneo R.** 2012. Base of the measles virus fusion trimer head receives the signal that triggers membrane fusion. J. Biol. Chem. **287:**33026–33035.
27. **Bose S, Zokarkar A, Welch BD, Leser GP, Jardetzky TS, Lamb RA.** 2012. Fusion activation by a headless parainfluenza virus 5 hemagglutinin-neuraminidase stalk suggests a modular mechanism for triggering. Proc. Natl. Acad. Sci. U. S. A. **109:**E2625–E2634.
28. **Plemper RK, Hammond AL, Cattaneo R.** 2000. Characterization of a region of the measles virus hemagglutinin sufficient for its dimerization. J. Virol. **74:**6485–6493.
29. **Plemper RK, Brindley MA, Iorio RM.** 2011. Structural and mechanistic studies of measles virus illuminate paramyxovirus entry. PLoS Pathog. **7:**e1002058. doi:10.1371/journal.ppat.1002058.
30. **Plemper RK, Hammond AL, Gerlier D, Fielding AK, Cattaneo R.** 2002. Strength of envelope protein interaction modulates cytopathicity of measles virus. J. Virol. **76:**5051–5061.
31. **Plemper RK, Hammond AL, Cattaneo R.** 2001. Measles virus envelope glycoproteins hetero-oligomerize in the endoplasmic reticulum. J. Biol. Chem. **276:**44239–44246.
32. **Plattet P, Langedijk JP, Zipperle L, Vandevelde M, Orvell C, Zurbriggen A.** 2009. Conserved leucine residue in the head region of morbillivirus fusion protein regulates the large conformational change during fusion activity. Biochemistry **48:**9112–9121.
33. **Buchholz UJ, Finke S, Conzelmann KK.** 1999. Generation of bovine respiratory syncytial virus (BRSV) from cDNA: BRSV NS2 is not essential for virus replication in tissue culture, and the human RSV leader region acts as a functional BRSV genome promoter. J. Virol. **73:**251–259.
34. **Ono N, Tatsuo H, Hidaka Y, Aoki T, Minagawa H, Yanagi Y.** 2001. Measles viruses on throat swabs from measles patients use signaling lymphocytic activation molecule (CDw150) but not CD46 as a cellular receptor. J. Virol. **75:**4399–4401.
35. **Seki F, Ono N, Yamaguchi R, Yanagi Y.** 2003. Efficient isolation of wild strains of canine distemper virus in Vero cells expressing canine SLAM (CD150) and their adaptability to marmoset B95a cells. J. Virol. **77:**9943–9950.
36. **Wyss-Fluehmann G, Zurbriggen A, Vandevelde M, Plattet P.** 2010. Canine distemper virus persistence in demyelinating encephalitis by swift intracellular cell-to-cell spread in astrocytes is controlled by the viral attachment protein. Acta Neuropathol. **119:**617–630.
37. **Doyle J, Prussia A, White LK, Sun A, Liotta DC, Snyder JP, Compans RW, Plemper RK.** 2006. Two domains that control prefusion stability and

transport competence of the measles virus fusion protein. J. Virol. **80:** 1524–1536.
38. **Singh M, Billeter MA.** 1999. A recombinant measles virus expressing biologically active human interleukin-12. J. Gen. Virol. **80**(Pt 1)**:**101–106.
39. **Duprex WP, McQuaid S, Roscic-Mrkic B, Cattaneo R, McCallister C, Rima BK.** 2000. In vitro and in vivo infection of neural cells by a recombinant measles virus expressing enhanced green fluorescent protein. J. Virol. **74:**7972–7979.
40. **Mastronarde DN.** 2005. Automated electron microscope tomography using robust prediction of specimen movements. J. Struct. Biol. **152:** 36–51.
41. **Kremer JR, Mastronarde DN, McIntosh JR.** 1996. Computer visualization of three-dimensional image data using IMOD. J. Struct. Biol. **116:**71–76.
42. **Heymann JB.** 2001. Bsoft: image and molecular processing in electron microscopy. J. Struct. Biol. **133:**156–169.
43. **Plemper RK, Compans RW.** 2003. Mutations in the putative HR-C region of the measles virus F2 glycoprotein modulate syncytium formation. J. Virol. **77:**4181–4190.
44. **Deng R, Mirza AM, Mahon PJ, Iorio RM.** 1997. Functional chimeric HN glycoproteins derived from Newcastle disease virus and human parainfluenza virus-3. Arch. Virol. Suppl. 13:115–130.
45. **Zwietering MH, Jongenburger I, Rombouts FM, van 't Riet K.** 1990. Modeling of the bacterial growth curve. Appl. Environ. Microbiol. **56:** 1875–1881.
46. **Rodgers JL, Nicewander WA.** 1988. Thirteen ways to look at the correlation coefficient. Am. Stat. **42:**59–66.
47. **Pearson K.** 1895. Note on regression and inheritance in the case of two parents. Proc. R. Soc. London **58:**240–242.
48. **Tahara M, Ito Y, Brindley MA, Ma X, He J, Xu S, Fukuhara H, Sakai K, Komase K, Rota PA, Plemper RK, Maenaka K, Takeda M.** 2013. Functional and structural characterization of neutralizing epitopes of measles virus hemagglutinin protein. J. Virol. **87:**666–675.
49. **Liljeroos L, Huiskonen JT, Ora A, Susi P, Butcher SJ.** 2011. Electron cryotomography of measles virus reveals how matrix protein coats the ribonucleocapsid within intact virions. Proc. Natl. Acad. Sci. U. S. A. **108:** 18085–18090.
50. **Harbury PB, Zhang T, Kim PS, Alber T.** 1993. A switch between two-, three-, and four-stranded coiled coils in GCN4 leucine zipper mutants. Science **262:**1401–1407.
51. **Corey EA, Iorio RM.** 2007. Mutations in the stalk of the measles virus hemagglutinin protein decrease fusion but do not interfere with virus-specific interaction with the homologous fusion protein. J. Virol. **81:** 9900–9910.
52. **Dutch RE.** 2010. Entry and fusion of emerging paramyxoviruses. PLoS Pathog. **6:**e1000881. doi:10.1371/journal.ppat.1000881.
53. **Mirza AM, Iorio RM.** 2013. A mutation in the stalk of the Newcastle disease virus hemagglutinin-neuraminidase (HN) protein prevents triggering of the F protein despite allowing efficient HN-F complex formation. J. Virol. **87:**8813–8815.
54. **Harrison MS, Sakaguchi T, Schmitt AP.** 2010. Paramyxovirus assembly and budding: building particles that transmit infections. Int. J. Biochem. Cell Biol. **42:**1416–1429.
55. **Li M, Schmitt PT, Li Z, McCrory TS, He B, Schmitt AP.** 2009. Mumps virus matrix, fusion, and nucleocapsid proteins cooperate for efficient production of virus-like particles. J. Virol. **83:**7261–7272.
56. **Pohl C, Duprex WP, Krohne G, Rima BK, Schneider-Schaulies S.** 2007. Measles virus M and F proteins associate with detergent-resistant membrane fractions and promote formation of virus-like particles. J. Gen. Virol. **88:**1243–1250.
57. **Liljeroos L, Krzyzaniak MA, Helenius A, Butcher SJ.** 2013. Architecture of respiratory syncytial virus revealed by electron cryotomography. Proc. Natl. Acad. Sci. U. S. A. **110:**11133–11138.